Fluid systems and fracture development during syn-depositional 1 fold growth: an example from the Pico del Aguila anticline, Sierras Exteriores, Southern Pyrenees, Spain.

Nicolas Beaudoin, Damien Huyghe, Nicolas Bellahsen, Olivier Lacombe, Laurent Emmanuel, Frédéric Mouthereau, Laure Ouanhnon

1 **Fluid systems and fracture development during syn-depositional fold growth: an**

2 **example from the Pico del Aguila anticline, Sierras Exteriores, Southern Pyrenees,**

3 **Spain.**

4

5 Nicolas Beaudoin[1,2,3,*], Damien Huyghe[4], Nicolas Bellahsen[1,2], Olivier Lacombe[1,2], Laurent

6 Emmanuel[1,2], Frédéric Mouthereau[1,2], Laure Ouanhnon[1,2].

7 [1] Sorbonne Universités,UPMC Univ Paris 06, UMR 7193, ISTEP, F-75005, Paris, France.
8 [2] CNRS, UMR 7193, F-75005, Paris, France.
9 [3] School of Geographical and Earth Sciences, University of Glasgow, Gregory Building,
10 G128QQ Glasgow, United Kingdom.
11 [4] UMR 5563 - Geosciences Environnement Toulouse, Université Paul Sabatier Toulouse
12 III, Toulouse, France.

13

16
17
18
19 **Abstract**

20

21 This paper reports an integrated, spatio-temporal analysis of the fracture-controlled

22 paleo-fluid system in the Pico del Aguila anticline, a N-S trending fold located in the

23 Sierras Exteriores, the southern front of the Spanish Pyrenees. Eight fracture sets (joints

24 or faults) are recognized throughout the fold and are separated into a fracture sequence

25 that is defined using field relationships and the remarkable temporal constraints offered

26 by the syn-tectonic sedimentary deposits. This fracture sequence records a complex

27 Paleocene to Early Oligocene structural evolution, including map-view, clockwise

28 rotation and tilting of the fold axis. The geochemical analysis of calcite cements from the

29 different mineralized fracture/vein sets reveals a compartmentalized fluid system

30 during most of fold development. This initial paleofluid system was later perturbed

31 when bending-related fractures associated with foreland flexure and outer arc extension

32 triggered small-scale, vertical fluid migration. Fractures developed in shallow strata

33 facilitated downward migration of surficial fluids that controlled the paleo-fluid system

34 in the Late Priabonian/Stampian continental deposits. The study of the Pico del Aguila

35 anticline depicts for the first time the evolution of a fluid system in a shallow, syn-

36 depositional compressional setting, and results further strengthen the statement that

37 fluids migrate vertically across stratigraphic boundaries take place during fold hinge-

38 related deformation.

39

40 **1. Introduction**

41 Fluid-rock interactions during folding control diagenesis and deformation, hydrocarbon

42 migration, and heat transport (Qing and Mountjoy, 1992; Roure et al., 2005; Katz et al.,

43 2006; Lacombe et al., 2014). A recent review of factors governing the temporal and

44 spatial distribution of fluids in folds (Evans and Fischer, 2012) highlights that the

45 development of a sub-seismic fracture network is essential in fluid migration. In

46 particular, the vertical persistence and lateral connectivity of joints usually promotes

47 alternating vertical and lateral fluid migrations at local and large-scale (e.g. Evans and

48 Battles, 1999; Van Geet et al., 2002; Fischer et al., 2009; Barbier et al., 2012a; Beaudoin

49 et al., 2011, 2014). Although no simple rule arises since each natural case of fold-

50 fracture-fluid interactions differs, a common characteristics occurs (Evans and Fischer,

51 2012): the development of curvature-related fracture sets promotes vertical fluid

52 migration and mixing of various preexisting hydrologic reservoirs delimited by

53 stratigraphic seals. This kind of evolution can be deciphered when both the large faults

54 and the fracture network are studied. Indeed, sub-seismic fracture patterns experience a

55 succession of deformation steps at fold-scale (Stearns and Friedman, 1972; Fischer and

56 Wilkerson, 2000; Bergbauer and Pollard, 2004; Bellahsen et al., 2006a, b; Cooper et al.,

57 2006; Tavani et al., 2006; Beaudoin et al., 2012, 2013). However, most studies were

58 performed in settings where deformation substantially postdates strata compaction

59 (Evans and Battles, 1999; Van Geet et al., 2002; Fischer et al., 2009; Beaudoin et al.,

60 2011, 2014; Barbier et al., 2012a). Consequently, the evolution of fluid-rock interactions

61 in strata folded at shallow depth during sediment deposition remains incompletely

62 documented.

63 Here, we study the case of the Pico del Aguila anticline, one of the N-S trending

64 folds of the Sierras Exteriores positioned at the southern structural front of the Pyrenees

65 (Fig. 1). The Pico del Aguila anticline is interpreted as a detachment fold with a

66 décollement level located within Triassic evaporitic rocks (Millán, 1996). The growth of

67 the structure is recorded by the syn-tectonic deposition of deep marine to continental

68 sediments from the Late Lutetian to Priabonian times (Millán et al., 1994; Hogan and

69 Burbank, 1996; Castelltort et al., 2003). The kinematics and mechanics of the Sierras

2

70   Exteriores and especially the Pico del Aguila anticline have been extensively

71   documented (Millán et al., 1994; Poblet and Hardy, 1995; Poblet et al., 1998; Novoa et

72   al., 2000; Anastasio and Holl, 2001; Castelltort et al., 2003; Nalpas et al., 2003; Huyghe et

73   al., 2009; Vidal-Royo et al., 2012, 2013). Our investigation of the fluid system in the

74   southernmost fold structures of the Pyrenean foreland allows a comparison with recent

75   studies of fluid systems in the northern hinterlandward fault-related folds (Travé et al.,

76   2000, 2007; Lacroix et al., 2011, 2014).

77   This contribution aims to describe the fracture network in the Pico del Aguila

78   anticline, and then using the remarkable record of fold evolution granted by the growth

79   strata to decipher the history of fracturing. Geochemical analyses of calcite vein cements

80   as well as fault-coating calcite are used to identify and interpret the sources of fluids that

81   flowed in fractures, their pathways, and their interactions with surrounding rocks.

82   Beyond regional implications, results shed light on the evolution of the paleo-fluid

83   system during growth of syn-depositional detachment folds.

84

85   **2. Geological Setting**

86

87   The Pico del Aguila anticline is a 160°E trending anticline located in the Sierras

88   Exteriores, a range comprising a set of NW-SE to N-S trending folds markedly oblique to

89   the south-Pyrenean thrust front (Fig. 1). The Sierras Exteriores are located at the

90   southern front of the Jaca piggyback basin, which borders the southwestern part of the

91   Central Pyrenees. The Pico del Aguila anticline plunges 30° toward the North, because it

92   is linked to the late thrusting of the Jaca Basin over the Ebro basin during the activation

93   of the Guarga basement thrust (Fig. 1B, Teixell, 1996; Jolivet et al., 2007). The Pico del

94   Aguila anticline is a detachment fold with a décollement level located within the Triassic

95   evaporite strata (Fig. 2). The growth of this anticline is well-constrained by the wealth of

96   biostratigraphic data (Canudo et al., 1988; Molina et al., 1988; Sztràkos and Castelltort,

97   2001; Huyghe et al., 2012a) and paleomagnetic studies (Hogan and Burbank, 1996)

98   obtained on Middle Eocene to Oligocene growth strata. The sedimentary succession (Fig.

99   1C) comprises dolostones and gypsiferous clays composing the Triassic Muschelkalk

100 and Keuper facies, respectively (Millán et al., 1994). The overlying formations are the

101 upper Cretaceous platform limestones of the Adraén-Bona Formation (Fm.), the

102 Paleocene continental and fluvial sandstones and mudstones of the Tremp Fm., and the

3

103 Lutetian shallow marine limestones of the Guara Fm. The sedimentary record indicates

104 that folding began during the deposition of the upper part of the Guara Fm. (upper

105 Lutetian, Millán et al., 1994; Huyghe et al., 2012a) and lasted during deposition of the

106 Bartonian-early Priabonian prodeltaic marls of the Arguis Fm. and the Middle-

107 Priabonian marine shallow-deltaic sandstone of the Belsué-Atarès Fm. This

108 interpretation is in accordance with the growth model of Hogan and Burbank (1996)

109 that indicates that folding began during the late Lutetian (42 Ma) and ended during early

110 Priabonian (35 Ma). On top of the latter formation, the Late Priabonian-Stampian

111 continental sandstones and claystones of the Campodarbe Fm. were deposited after

112 folding (Millán et al., 1994). Subsequent thrusting of the Jaca basin over the Ebro basin is

113 due to the development of the southern Pyrenean frontal thrust during Late Oligocene-

114 early Miocene (Millán, 1996; Jolivet et al., 2007; Huyghe et al., 2009).

115

116 3. Methodology to decipher fluid-fracture-fold evolution

117

118 This work focuses on fracture generations observed in pre-, syn- and post-folding

119 strata of the Pico del Aguila anticline. Fracture generations are mainly composed of

120 joints and veins opened in mode I, as well as faults along which movement is recorded

121 by slickensides. Pressure-solution seams (stylolites) related to both compaction and

122 tectonic loading also occur. Mode I-opening of joints and veins was checked in the field

123 and in thin-sections by the offset of pre-existing elements in the matrix or by the lack of

124 grain crushing in the matrix near the borders of the fractures (Fig. 3a).

125 Nearly 1500 joint/vein orientation data were collected along with 120 fault-slip data at

126 the outcrop-scale (Fig. 4-7, Table S2 as supplementary material) in different formations

127 (pre-, syn-, and post-folding strata extending from Triassic to Priabonian) and structural

128 positions (hinge and limbs). About 50 sites were defined by a common structural

129 position and bedding dip, half of them being located in the pre-folding strata (25 sites).

130 The post-folding strata of the Campodarbe Fm. have fewer samples in our dataset (6

131 sites).

132

133 3. 1. Identification of fracture sets

134 Identification of fracture sets is now a well-established and powerful tool to

135 unravel the deformation history of folded strata (eg, Bergbauer and Pollard, 2004;

136 Bellahsen et al., 2006; Lacombe et al., 2012). Fracture sets can be defined as fracture

137 populations that share a common deformation mode, a common orientation regarding

138 the bedding dip and with statistically consistent chronological relationships compared

139 to other fracture sets. For our study, we compute the mean orientation of measured

140 fractures for each site by means of a Kernel statistical analysis (software developed at

141 IFPEN for the definition of fracture sets, see Bellahsen et al., 2006; Ahmadhadi et al.,

142 2008). This data processing is first done for the present position of strata, then after the

143 correction of the fold axis plunge (by removing the tilt of 30° due to the frontal thrust

144 activity), and in a third step after the removal of the local bedding dip. Results are

145 presented on stereonets for each measurement site at each step (Figs. 3 to 6). Diagrams

146 are not weighted by abundance, as we believe that this modification can be biased by

147 outcrop conditions. However, vertical persistence, spacing or relative abundance of

148 fractures all were considered for the interpretations. Indeed, we believe that a fracture

149 set is relevant to constrain the tectonic evolution of strata only if it is observed

150 everywhere in the fold, or at least in numerous sites from a single structural or

151 stratigraphic position. Therefore, data processing results in the recognition of different

152 fracture sets that are each related to a deformation event. We assume that the

153 development of a fracture set will not overlap the development of another fracture set

154 except if the stress conditions required are similar for these two sets and if

155 chronological relationships suggest synchronism. Consequently, we use chronological

156 relationships to constrain the development of fracture sets through time so to build the

157 fracture sequence.

158   Four approaches are used to determine the relative age of the different fracture

159 sets: (a) the relative age of fractures based on abutting or offset relationships at field

160 sites; (b) the restriction of fractures to particular units in the pre-, syn- and/or post-

161 folding stratigraphic sequence; (c) the assumption that mode I fractures formed

162 vertically with a horizontal least compressive principal stress (Anderson, 1951); and (d)

163 the assumption that bed-perpendicular fractures striking parallel to the fold axis and

164 located near the hinge of the fold are related to local extension due to strata bending. We

165 carefully observed abutments and crosscutting relationships on pavements at the Pico

166 del Aguila, using a rule that a set composed of fractures that terminate at fractures of

167 another set are inferred to have developed later (Fig. 8). These relationships observed at

168 site-scale are checked on thin sections, and the consistency of the chronology is checked

169 at the fold-scale. Finally, the sequence is checked with the record provided by growth

170 strata.

171

172 *3.2. Inversion of fault-slip data for paleostress*

173

174 Some fracture sets comprise only faults, which slips were inverted to reconstruct

175 the related stress tensor using the inversion methods described in Angelier (1984)(see

176 Lacombe, 2012 for a recent review of fault-slip data inversion for paleostresses). The

177 identification and separation of successive generations of faults and related stress

178 regimes are based on both mechanical incompatibility between individual fault slips

179 (with the computed stress tensor) and relative chronology observations (e.g.,

180 superimposed striations on fault surfaces, crosscutting relationships between faults). As

181 with the fracture sets, we provide stereonets to show the results of fault-slip data

182 inversion (1) in the current strata attitude (post-thrusting); (2) after removing the

183 regional tilt of the fold axis due to the activation of the frontal thrust (pre-thrusting and

184 post-folding); (3) and after removing the local bedding dip (pre-folding). If one assumes

185 that a principal stress axis remains generally vertical without local stress rotations,

186 which could be due to stress channelization within shallow-dipping strata separated by

187 low friction interlayers along which bedding-parallel slip occurs (Tavani et al., 2006), (1)

188 inversion of a fault set formed before folding (or thrusting) and measured in a fold limb

189 would have one of the computed stress axes perpendicular to bedding, with the other

190 two lying in the bedding plane; (2) inversion of a post-folding or post-thrusting fault set

191 yields stress tensors with compression horizontal irrespective of bedding dip in the

192 current or pre-thrusting attitude (e.g., Lacombe, 2012). Note that pre-folding stress

193 tensors are presented on Schmidt's stereonets only in cases where stress axes are

194 consistent with these Andersonian conditions once corrected from plunge and/or

195 bedding dip.

196

197 *3.3. Petrographic and geochemical analyses of veins and host-rock cements*

198 Samples of vein calcite cements and fault-coating calcite within their surrounding

199 matrix were collected in a variety of stratigraphic and structural positions. We use

200 standard and cathodoluminescence petrography, as well as stable isotopes of carbon

201 and oxygen to constrain the geochemistry of the fluids from which calcite precipitated.

202 Although we observe fluid inclusions in the samples, microthermometric work proved

203 fruitless, and yielded only the observation that the inclusion population was dominated

204 by monophase (liquid), aqueous inclusions (Fig 3 e-f) where the attempts to nucleate

205 vapor bubble by freezing failed. Lack of vapor bubble in inclusions suggests a

206 precipitation of fluids about $80 \pm 20°C$ (Roedder, 1984).

207

208 Petrographic and cathodoluminescence observations were conducted on

209 oriented thin-sections of 35 selected samples that are representative of fracture sets

210 observed at the Pico del Aguila anticline. We use observations of vein crystal textures

211 and offset wall-rock markers to constrain the mode of fracture wall displacement (Fig.

212 3). Microscopy also allowed checking and refining the chronological relationships that

213 have been initially defined from field observations. We use a Cathodyne Opea cold

214 cathode system to examine the cathodoluminescence of the samples (Fig. 9). These

215 observations constrain the number of precipitation events, the conditions of

216 precipitation, and the diagenesis of the veins and host rocks. Operating conditions are in

217 the range of 200–400 lA and 13– 18 kV gun current with a constant 60 mTorr vacuum.

218

219 $\delta^{18}O$ and $\delta^{13}C$ have been measured in calcite collected from 70 veins and related

220 host-rocks, covering various structural and stratigraphic positions in the Pico del Aguila

221 anticline (Fig. 10, Table S1). Measurements are performed using an automated

222 preparation device coupled to an Isoprime gas-ratio mass spectrometer. Between 40

223 and 100 μg of calcite powder is collected from each veins, using either hand-drill or

224 scalpel to avoid mixture with host-rocks. Samples are placed in glass vials and reacted

225 with dehydrated phosphoric acid under vacuum at 90°C, before being measured 10

226 times each. A correction for dolomite samples was conducted (Rosenbaum and

227 Sheppard, 1986). Hereinafter, all values for both veins and host-rocks are reported in

228 per mil (‰) relative to the Vienna Pee Dee Belemnite (VPDB or PDB) for carbon and for

229 oxygen with an accuracy of 0.05‰ and 0.1‰, respectively (Table S1).

230

231 **4. Fracture system: observations and interpretations**

232

233 We present a new geological map, based on recent field observations and high-

234 resolution aerial photographs that slightly differs from the previous maps (Fig. 2; e.g.

7

235 Puigdefabregas, 1975; Millán, 1996; Vidal-Royo et al., 2012). The main difference is that

236 Triassic rocks are not observed in the northern part of the fold where sub-vertical

237 limestone strata of the Cretaceous Adraen-Bona Fm. were observed.

238   Eight fracture sets are defined by field observations, statistical analyses, and stress

239 inversion processes, including 5 joint/vein sets (Figs. 4-6) and 3 striated fault sets (Fig.

240 7). For the sake of simplicity, the fracture sequence is presented with a nomenclature

241 defined by relative timing with respect to folding (Fig. 8).

242   Sets J1 and J2 appear mainly in the oldest pre-tectonic formation (Table 1, figs. 4-5-

243 6), making them the oldest fractures to have developed. Both are bed-perpendicular.

244 Once the plunge and local dip are removed, set J1 strikes 120° while set J2 strikes 090°.

245 Cross-cutting relationships show younger J2's abutting against older J1's (Fig. 8-b).

246 Other sets are observed in all stratigraphic units. Set J3 joints and veins strike 070° and

247 are bed-perpendicular, and abut against set J2 fractures (Fig. 8-c). Set J4 joints and veins

248 strike 40° and are bed-perpendicular, reopen J3 fractures and abut against J2 fractures

249 (Fig. 8-c). Sets J3 and J4 are observed in every structural position, whereas set J5 is only

250 observed near the anticline hinge and in the syncline. Set J5 joints and veins are roughly

251 normal to bedding and strike mainly 170°. Chronological relationships from outcrops

252 and thin sections indicate that set J5 is younger than sets J1, J2, J3, and J4 (Fig 8-a,d),

253 whereas chronological relationships with set J4 are ambiguous.

254   Sets F1, F2 and F3 comprise faults that are defined by a common causative

255 paleostress reconstructed using a stress inversion process (Fig. 7). Because the lack of

256 crosscutting relationships, the chronology of these fault sets is poorly constrained by

257 field and petrographic observations. Age of the fault sets with respect to folding and

258 thrusting events can however be assessed by assuming that they developed when the

259 stress tensor has a vertical principal stress, as predicted by Anderson (1951). Set F1

260 comprises steeply dipping, N-S striking normal faults that were only observed at the fold

261 hinge, and developed under an E-W extensional stress regime during folding (Fig. 7). Set

262 F2 comprises newly-formed N-S reverse faults (ex: site 434, Fig. 7) with strike-slip

263 reactivation of fractures oriented 045°E/060°E (ex: site 433-2, Fig. 7) and 160° (ex: 474,

264 Fig. 7), and are compatible with a nearly E-W compression which respect to Anderson's

265 theory in the current attitude of strata or just plunge-corrected, meaning they developed

266 since post-folding. Lastly, set F3 comprise a group of conjugate E-W reverse faults that

267 formed in a predominantly N-S compressional stress regime (ex: site 136-1, Fig. 7).

8

268 These faults developed after folding, some of them postdate thrust activation (ex: site

269 136-1, Fig. 7) while the observed orientation, motion and steep angle of some other

270 reverse faults (ex: site 34, Fig. 7) suggests that they developed at a lower angle during

271 the thrusting.

272

273   Prior work has shown that the area of the southern Pyrenean thrust front

274 experienced rotation around a vertical axis. This rotation is interpreted as being related

275 to the southwestward propagation of the deformation in the south Pyrenees and is

276 believed to partially explain the N-S striking of the folds in the Sierras Exteriores.

277 Rotations of 15° to 50° have been proposed from paleomagnetic studies (Pueyo et al.,

278 2002; Oliva-Urcia and Pueyo 2007) and on displacement field reconstruction (Huyghe et

279 al., 2009). Timing of such a rotation for the Pico del Aguila area is inferred to have

280 started as soon as Bartonian and terminated during Oligocene times (Huyghe et al.,

281 2009).

282   Consequently, this rotation history is of primary importance for interpreting the

283 fracture sequence with respect to anticline development (Fig.11). Drawing on timing of

284 sedimentation with respect to folding (Fig. 1B), and on the stratigraphic distribution of

285 the fracture sets (Figs. 3 to 8, Table 1), we propose that the progressive development of

286 fractures from a 090° strike (set J2 only in oldest strata) to a 040° strike (set J4 in all

287 strata) reflects a progressive clockwise rotation (Fig. 11). Joint sets J2 to J4 are inferred

288 to have formed sequentially parallel to the direction of maximum contraction as part of

289 the structural suite recording regional layer-parallel shortening (LPS) that we here

290 documented as striking NE-SW (Fig. 11-a-b-c (2)). This interpretation is based on (1) the

291 established existence of a rotation in the area, (2) the fact that set J2 is a bed-

292 perpendicular, fold-axis perpendicular-striking set of joints which can be related to LPS

293 (e.g. Bellahsen et al., 2006a), and (3) the stratigraphic distribution of fracture sets,

294 where J2 is observed only in prefolding and prerotation Guara Fm. (Huyghe et al., 2009)

295 while J3 and J4 developed also in syn-rotation strata (Table 1). The angular difference in

296 present-day strikes for sets J2 to J4 is 50°, which we infer to reflect the maximum

297 magnitude of the rotation around a vertical axis (Fig.11-a-b-c). Our interpretation differs

298 from previous work that predicts a rotation of only 20° at the Pico del Aguila (Huyghe et

299 al., 2009). Considering our data, because of possible local heterogeneities and bed-scale

300 stress perturbations, the strikes of fracture sets are only given within 10° of accuracy

9

301 (Table 1). Given this limitation and considering mean strikes for each fracture set, the

302 minimal value for the vertical rotation is the difference between J2's (80°) and J4's (50°)

303 strikes. Therefore, our dataset suggests a vertical rotation of about 30° and is more

304 likely considering results from other studies (Pueyo et al., 2002; Oliva-Urcia and Pueyo

305 2007, Huyghe et al., 2009).

306   We infer that set J1 predates the rotation and its final orientation fully records

307 the rotation. Given a present day strike of 120°, the regional trend of J1 before the

308 rotation would be 090° (Fig. 11-a (1)). Thus, the joints could be interpreted as having

309 developed during N-S extension related to foreland flexure and/or forebulge in the area

310 (Hervouët et al., 2005). Set J5 is inferred to have developed at the anticline hinge during

311 outer-arc bending that occurred during vertical axis rotation. As these fractures reflect

312 hinge-related deformation, their orientation remained parallel with the anticlinal hinge

313 as it rotated (Fig. 11 a-b-c). Similarly, during fold growth, hinge extensional strain was

314 accommodated by development of F1 faults that were also rotated with the anticline as

315 it grew and spun (Fig. 11-c (3)). Crosscutting relationships between J4 and J5 are

316 ambiguous, so the development of J4 fractures parallel to regional contraction could

317 have been before or coeval with local extension at the hinge.

318   After rotation around a vertical axis was completed (Fig. 11-d (4)), fold tightening

319 locally perturbed tectonic stress that became perpendicular to fold axis (e.g., Amrouch et

320 al., 2010), in response to which set F2 formed. Later, the Pyrenean-related N-S

321 contraction triggered E-W-trending thrusts ramps (Teixell, 1996; Jolivet et al., 2007),

322 tilted the folds axis during its overthrusting above the 30°-dipping frontal ramp and

323 caused E-W small reverse F3 faults (Fig. 11-d (5)).

324   The proposed fracture sequence reflects a tectonic history starting from foreland

325 flexure and/or forebulge until the late activation of regional thrusts due to Pyrenean N-S

326 orogenic contraction. Similar relationships between regional-scale foreland flexure and

327 the development of systematic sets of parallel joints/veins have been proposed in other

328 foreland basins (Billi and Salvini, 2003; Beaudoin et al., 2012; Quintà and Tavani, 2012),

329 and supports a growing body of evidence that many fractures observed in folded strata

330 may in fact predate folding history (e.g., Bergbauer and Pollard, 2004; Bellahsen et al.,

331 2006a; Ahmadhadi et al., 2008; Lacombe et al., 2011; Quinta and Tavani, 2012).

332

333 **5. Fluid system: observations and interpretations**

334

335   *5.1. Sample selection according to microstructural observations*

336   Using observations of veins and surrounding host-rocks from optical and

337   cathodoluminescence microscopy (Fig. 3, 9), four different textures in veins can be

338   described, following the classifications of Durney and Ramsay (1973) and Machel

339   (2000).

340   The textures are (1) blocky calcite with single-phase, bright orange luminescence with

341   brighter fringes at the external rim of crystals (Fig. 9-a); (2) blocky calcite with grain-

342   scale luminescence zonation from bright to dull orange luminescence (Fig. 9-b); (3)

343   Elongated blocky veins with orange luminescence variation in the vein while each

344   fibrous crystal has homogeneous luminescence (Fig. 9-c); and (4) Crack-seal textures

345   characterized by fringes of fine stretched grains on the outer bound of the vein

346   recording one single (Fig. 3-d) or multiple (Fig. 3-a) events. The four textures are

347   observed in all veins sets, so correlation does not exist between texture and either with

348   stratigraphic position or structure or vein set, suggesting precipitation mechanisms

349   independent from these parameters.

350   Textures in veins can be used as indicators of mode I opening and for a single

351   event of fluid precipitation. Blocky calcite texture showing growth competition (Fig. 3-d)

352   is symptomatic of a single fluid precipitation event (Bons et al., 2012). Most of veins

353   from our samples displays such a texture, and cathodoluminescence observed in case

354   (1) (Fig. 9-a) is related to dynamic recrystallization due to growth competition (Machel,

355   2000), while small-scale zonation of case (2) reflects slower precipitation under variable

356   redox condition or simply variation in precipitation kinetics (Machel, 2000). Elongated

357   blocky veins described as texture (3) (Figs. 3-b, 9-c) can be interpreted to reflect

358   precipitation kinetics of fluid equivalent to opening kinematics of the fracture (Bons et

359   al., 2000). Also, the elongation direction relates to the direction of opening of veins, and

360   is useful to distinguish mode I veins fractures (Fig. 3-b) from oblique opening veins

361   fractures (Fig. 3-a), where the latter were discarded from our geochemical study. Finally,

362   multiple crack-seal events were discarded for geochemistry (Fig. 3-a) as they reflect

363   multiple or discontinuous fluid precipitation events, possibly involving different sources

364   (Bons et al. 2000).

365

366   *5.2. Fluid sources from isotopic measurements*

367   To interpret the geochemical dataset in terms of fluid system evolution, we
368   divided the data into pre-, syn-, and post-folding groups based on host stratigraphic
369   units to determine if isotopic data from veins and host rock show correlations with
370   stratigraphy and/or fold timing (Fig. 10, Table 2). Considering the data this way, we
371   identify four patterns: (1) Veins from Triassic Fms. and some veins from pre-folding
372   Guara Fm. exhibit $\delta^{18}O$ and $\delta^{13}C$ values lower than those of their host-rocks; (2) all other
373   veins belonging to pre-folding formations exhibit $\delta^{18}O$ values lower than those of their
374   host-rocks, while simultaneously exhibiting $\delta^{13}C$ values that are broadly similar to those
375   of their host-rocks. (3) Veins in the syn-folding Arguis Fm. have $\delta^{18}O$ and $\delta^{13}C$ similar to
376   their host-rock values. (4) Veins from the post-folding Campodarbe Fm. exhibit $\delta^{18}O$
377   values that are significantly greater than their host-rock values, but $\delta^{13}C$ values similar
378   to their host-rock values. These four patterns in the data suggest that fluids from
379   different sources interacted with the host-rocks before, during and after folding, such
380   that fluid flow and precipitation were a function of stratigraphic interval and
381   deformation timing.

382   Isotopic disequilibrium in vein cements that belong to pattern (1) suggests an
383   opening of each reservoir to an external source of fluids, characterized by negative $\delta^{13}C$
384   values. As shown in Fig. 10-a, the low $\delta^{13}C$ values in some Guara Fm. and Triassic veins
385   seem to match those of host rocks in the Paleocene Tremp Fm, and we note that the
386   negative $\delta^{13}C$ values are consistent with sedimentary rocks inferred to represent
387   paleosoils and lakes (Pujalte et al., 2009) that contain organic matter. The shallow burial
388   depth attained in this area makes it unlikely that the lower $\delta^{13}C$ values in veins reflect
389   the influence of hydrocarbons. Instead, we infer paleohydrological connection and
390   mixing between fluids from these Paleocene and Triassic units. Interestingly, this
391   connection is recorded broadly in veins of sets J1 and J5, meaning that most of the
392   vertical fluid migration between units was triggered by curvature-related fractures,
393   either due to folding or to regional foreland flexure (Fig. 12-a).

394   Isotopic patterns of cases (2) and (3) reflect a closed stratified fluid system that
395   experienced a different evolution regarding the timing of deposit of host-rock regarding
396   evolution of folding (Fig. 10-a,-b):
397   - Veins in pre-folding formations that are not case (1) can be defined by isotopic pattern
398   (2). The lower $\delta^{18}O$ of veins relative to host rocks can be interpreted resulting from
399   precipitation of local fluids after a burial (e.g. Ferket et al., 2000; Travé et al., 2007; Fitz-

400 Diaz et al., 2011; Evans et al., 2012; Vandeginste et al., 2012). According to the isotopic

401 difference between veins and host-rocks (Δ on Fig. 10-b) and considering temperature-

402 dependent fractionation between H_2O and $CaCO_3$ after Kim and O'Neil (1997), we

403 estimate that pore fluids precipitated 30°C higher than host-rock precipitation

404 temperature. Considering "normal" geothermal gradient, this interpretation implies a

405 burial of 1km, consistent with the sedimentary history (Vidal-Royo et al., 2012).

406 - Syn-folding formation is characterized by an isotopic equilibrium between veins and

407 host-rocks (case (3)) that reflects local pore-fluids precipitation without significant

408 change in temperature since host-rock underwent diagenesis. This is consistent with the

409 limited burial experienced by the Arguis Fm. after it deposited in the area of the Pico del

410 Aguila (Millán, 1996).

411   The isotopic pattern of case (4) in the post-folding Campodarbe Formation is

412 inferred to represent an opening to external source of fluids characterized by a higher

413 $\delta^{18}O$ values. According to the continental paleo-environmental conditions at that time

414 (Millán, 1996), such a source could be either river-derived fluid or meteoric fluids. As

415 river-derived fluids isotopic range cannot be used to explain the measured signatures (-

416 8‰ to -5.5‰PDB, Zamarreno et al., 1997, Huyghe et al., 2012b), we propose that

417 isotopic signatures of case (4) record precipitation from meteoric fluids.

418

419 **6. Discussion : fluid-rock evolution during syn-depositional folding**

420

421   In their recent review focusing on fold-related fluid systems, Evans and Fischer

422 (2012) stressed the fact that these fluid systems have some common characteristics

423 before and during folding. Analysis of paleo-fluid systems during growth of both

424 detachment and basement-cored folds show that fluid systems are compartmentalized

425 by stratigraphy and exhibit little vertical fluid migration. During subsequent folding,

426 syn-folding joints and faults rupture stratigraphic seals and trigger vertical fluid

427 migration and mixing.

428   The fluid system evolution of the Pico del Aguila (Fig. 12-a) is accordingly

429 interpreted as a stratified fluid system during most of the geological history, with a

430 strong control of lithology on the fluid isotopic signatures (e.g. Fischer et al., 2009; Evans

431 and Fischer, 2012). However, inter-formational fluid flow is documented for sets J1 and

432 J5, which are related to flexural forebulge and local extension due to folding,

13

433 respectively. Once the paleo-environment switches from marine to continental during

434 Priabonian (Millán, 1996), the source for formational fluid switched from marine-

435 derived pore fluids to surficial, likely meteoric-derived fluids.

436 The likely common opening of fluid systems to vertical migration during folding

437 (e.g., Evans and Fischer, 2012, Fig.12) is therefore once more supported by the Pico del

438 Aguila case study. Opening during flexural forebulge has also been documented in the

439 Bighorn Basin (Beaudoin et al., 2014). Being the first syn-depositional fold developed at

440 shallow depth for which the fluid system has been studied, the Pico del Aguila

441 additionally illustrates, beyond the strong lithological control on the fluid system, the

442 progressive switch from marine to continental environment as documented by $\delta^{18}O$

443 values of calcite-cemented veins. This interpretation is consistent with observations of

444 current fluid flow in anticlines developed at shallow or significant water depth as in the

445 Central Basin in Iran or in Brunei (Morley et al., 2014). The difference in burial depth at

446 the time of deformation also impacts on the scale of the vertical migration triggered by

447 effective tension-related fracture sets (Fig. 12). For example in a deep buried basement-

448 cored fold, such as the Sheep Mountain anticline (Fig. 12-a, Beaudoin et al., 2011),

449 curvature-related fractures developed enough vertical permeability to allow fluid from

450 depth to invade all the strata, while such big-scale migration is not recorded for the Pico

451 del Aguila (Fig. 12-b). This difference could be directly related to the limited burial and

452 related mechanical compaction of the reservoir, and could illustrate the influence of

453 mechanical properties of strata on hydraulic behavior of curvature related fractures, as

454 highlighted in numerous natural cases (Cooke, 1997; Fischer and Jackson, 1999;

455 Laubach et al, 2009; Savage et al., 2010; Barbier et al., 2012a; b; Morley et al., 2014).

456 More generally, studies of regional fluid flows in the southern Pyrenean foreland

457 depict large-scale flows of hydrothermal fluids in structures closer to the Pyrenean

458 range (Travé et al., 2000; 2007), and in the Gavarnie thrust, structurally above the

459 Guarga thrust (McCaig et al. 1995; Henderson and McCaig, 1996; McCaig et al., 2000). In

460 the Pico del Aguila, no hydrothermal fluid flow overprinted the system during activation

461 of the underlying Guarga thrust that developed set F3 faults, in which syn-kinematic

462 calcite coating precipitated from local fluids (Table S1). The lack of evidence of deep

463 fluid flow has also been documented along the thrust system of the Monte Perdido,

464 South of Gavarnie (Lacroix et al., 2011) and can be related to the large distance from the

465 range (Figure 1, Lacroix et al., 2014). Alternatively, this lack could be related to limited

466 faults and joints development after folding. The related vertical permeability creation
467 was too limited and prevented fluids from the basement to flow through the non-
468 permeable evaporites underlying the limestone. Such a case is opposed to what can
469 happen in a basement-cored fold (Fig. 12-a).
470
471 **7. Conclusions**
472
473   1. The sub-seismic fracture pattern recognized in folded strata of the Pico del
474 Aguila anticline comprises 8 sets of joints/veins and faults. The oldest fracture set is
475 likely related to the regional-scale foreland flexure that affected strata during Lutetian
476 and therefore clearly predates folding history. Three fracture sets (J2 to J4) then
477 developed in progressively youngering strata, recording a clockwise vertical-axis
478 rotation of the area. Their E-W to NE-SW trends indicate that they developed under a
479 far-field, relatively static NE-SW shortening during the 30-40° rotation around a vertical
480 axis. Among the four remaining sets, two are related to local outer-arc extension during
481 folding (sets J5 and F1), one is related to E-W compression during late-stage fold
482 tightening (set F2), and the last is a set of post-thrusting faults (set F3) that formed in
483 the same N-S compressional stress regime that activated the Guarga basement thrust.
484   2. The paleo-fluid system related to the fracture pattern is stratified and
485 controlled by depositional environments during most of the history of vein mineral
486 precipitation. The development of regional-scale foreland flexure and local-scale strata
487 curvature-related vein sets triggered small-scale, interformational, vertical fluid
488 migrations between Triassic and Paleocene reservoirs. The progressive switch from
489 marine to continental paleo-environment occurring during Priabonian is recorded by a
490 change of fluid source from local marine fluids to terrestrial surficial fluids.
491   3. Our interpretation of the fluid system in the Pico del Aguila anticline supports
492 the hypothesis that fluid systems exhibit a common behavior during folding, wherein
493 curvature-related joints facilitate vertical migration of fluids from one
494 hydrostratigraphic reservoir to another. It also illustrates that the extent of such a
495 vertical migration may be strongly reduced when folding affects poorly compacted
496 sediments. Other similar case studies are needed to confirm if the fluid system evolution
497 deciphered in the Pico del Aguila anticline is archetypal of fold-related fluid systems in
498 shallow, syn-tectonic sedimentary settings.

15

499

Acknowledgments

506

References

509 Ahmadhadi, F., Daniel, J.M., Azzizadeh, M., Lacombe O., 2008. Evidence for pre-folding vein development in
510   the Oligo-Miocene Asmari Formation in the Central Zagros Fold Belt, Iran. Tectonics 27, TC1016,
511   doi:10.1029/2006TC001978

512 Anderson, E. M., 1951. The Dynamics of Faulting and Dyke Formation with Application to Britain. Oliver &
513   Boyd, Edinburgh.

514 Angelier, J., 1984, Tectonic analysis of fault slip data sets. Journal of Geophysical Research 89, 5835–5848.

515 Amrouch, K., Lacombe, O., Bellahsen, N., Daniel, J.-M., Callot, J.-P., 2010. Stress and strain patterns,
516   kinematics and deformation mechanisms in a basement-cored anticline: Sheep Mountain Anticline,
517   Wyoming. Tectonics 29, TC1005, 1–27, doi:10.1029/2009TC002525 .

518 Anastasio, D.J., Holl, J.E., 2001. Transverse fold evolution in the External Sierra, southern Pyrenees, Spain.
519   J. Struct. Geol. 23, 379–392.

520 Barbier, M., Leprêtre, R., Callot, J.-P., Gasparrini, M., Daniel, J.-M., Hamon, Y., Lacombe, O., Floquet, M.,
521   2012a. Impact of fracture stratigraphy on the paleo-hydrogeology of the Madison Limestone in two
522   basement-involved folds in the Bighorn basin, (Wyoming, USA). Tectonophysics, thematic issue :
523   « Into the deformation history of folded rocks » , O. Lacombe, S. Tavani, R. Soto (eds), 576–577, 116-
524   132.

525 Barbier, M., Hamon, Y., Callot, J.-P., Floquet, M., Daniel, J.-M., 2012b. Sedimentary and diagenetic controls
526   on the multiscale fracturing pattern of a carbonate reservoir: The Madison Formation (Sheep
527   Mountain, Wyoming, USA). Mar. Pet. Geol. 29, 50–67.

528 Beaudoin, N., Bellahsen, N., Lacombe, O., and Emmanuel, L., 2011. Fracture-controlled paleohydrogeology
529   in a basement-cored, fault-related fold: Sheep Mountain Anticline, Wyoming, United States.
530   Geochemistry Geophysics Geosystems 12, Q06011, doi: 10.1029/2010GC003494.

531 Beaudoin, N., Bellahsen, N., Lacombe, O., Emmanuel, L., Pironon, J., 2014. Crustal-scale fluid flow during
532   the tectonic evolution of the Bighorn Basin (Wyoming, USA). Basin Research 26, 403-435.

533 Beaudoin, N., Lacombe, O., Bellahsen, N., Emmanuel, L., 2013. Contribution of Studies of Sub-Seismic
534   Fracture Populations to Paleo-Hydrological Reconstructions (Bighorn Basin, USA). Procedia Earth
535   Planet. Sci. 7, 57–60.

536 Beaudoin, N., Leprêtre, R., Bellahsen, N., Lacombe, O., Amrouch, K., Callot, J.-P., Emmanuel, L., Daniel, J.-M.,
537   2012. Structural and microstructural evolution of the Rattlesnake Mountain Anticline (Wyoming,
538   USA): new insights into the Sevier and Laramide orogenic stress build-ups in the BigHorn Basin.
539   Tectonophysics, thematic issue : « Into the deformation history of folded rocks » , O. Lacombe, S.
540   Tavani, R. Soto (eds), 576–577, 20-45.

541 Bellahsen, N, Fiore, P., Pollard, D., 2006a. The role of fractures in the structural interpretation of Sheep
542   Mountain Anticline, Wyoming. J. Struct. Geol. 28, 850–867.

543 Bellahsen, N., Fiore, P., Pollard, D., 2006b. From spatial variation of fracture patterns to fold kinematics: A
544   geomechanical approach. Geophysical Research Letters 33, L02301, doi:10.1029/2005GL024189.

545 Bergbauer, S., 2007. Testing the predictive capability of curvature analyses. Geol. Soc. London, Spec. Publ.
546   292, 185–202.

547 Bergbauer, S., Pollard, D.D., 2004. A new conceptual fold-fracture model including prefolding joints, based
548   on the Emigrant Gap anticline, Wyoming. Geol. Soc. Am. Bull. 116, 294 – 307.

549 Billi, A., Salvini, F., 2003. Development of systematic joints in response to flexure-related fibre stress in
550   flexed foreland plates: the Apulian forebulge case history, Italy. J. Geodyn. 36, 523–536.

551 Bodnar, R., 1993. Revised equation and table for determining the freezing point depression of H2O-Nacl
552   solutions. Geochimica et Cosmochimica Acta 57, 683–684.

553 Boles, J. R., Eichhubl, P., Garven, G., Chen, J, 2004. Evolution of a hydrocarbon migration pathway along
554   basin-bounding faults: Evidence from fault cement. AAPG Bull. 88, 947–970.

555 Bons, P., Elburg, M. A>, Gomez-Rivas, E., 2012. A review of the formation of tectonic veins and their
556   microstructures. Journal of Structural Geology 43, 33-62.

557 Canudo, J.-I., Molina, E., Riveline, J., Serra-Kiel, J., Sucunza, M., 1988. Les èvènements biostratigraphiques
558   de la zone prépyrénéenne d'Aragon (Espagne), de l'Eocène Moyen à l'Oligocène Inférieur. Revue de
559   Micropaléontologie 31, 15-29.

560 Castelltort, S., Guillocheau, F., Robin, C., Rouby, D., Nalpas, T., Lafont, F., Eschard, R., 2003. Fold control on
561   the stratigraphic record: a quantified sequence stratigraphic study of the Pico del Aguila anticline in
562   the south-western Pyrenees (Spain). Basin Research 15, 527-551.

563 Cooke, M., 1997. Predicting fracture localization in folded strata from mechanical stratigraphy and fold
564   shape: Case study of east Kaibab Monocline, Utah. Int. J. Rock Mech. Min. Sci. 34, 56.

565 Cooper, S.P., Goodwin, L.B., Lorenz, J.C., 2006. Fracture and fault patterns associated with basement-cored
566   anticlines: The example of Teapot Dome, Wyoming. Am. Assoc. Pet. Geol. Bull. 90, 1903–1920.

567 Durney, D.W., Ramsay, J.G., 1973. Incremental stramsmeasured by syntectomc crystal growths In Gravtty
568   and Tectomcs (edited by De Jong, K A and Scholten. R) John Wdey, New York, 67-96.

569 Evans, M. A., Bebout, G.E., Brown, C.H., 2012. Changing fluid conditions during folding: An example from
570   the central Appalachians. Tectonophysics 576–577, 99–115.

571 Evans, M. A., Fischer, M.P., 2012. On the distribution of fluids in folds: A review of controlling factors and
572   processes. J. Struct. Geol. 44, 2–24.

573 Evans, M., Battles, D., 1999. stable isotope analyses of veins from the central Appalachian Valley and Ridge
574   province: Implications for regional synorogenic hydrologic structure and fluid migration. Geol. Soc.
575   Am. Bull. 111, 1841–1860.

576 Ferket, H., Roure, F., Swennen, R., Ortuno, S., 2000. Fluid migration placed into the deformation history of
577   fold-and-thrust belts: an example from the Veracruz basin (Mexico). Journal of Geochemical
578   Exploration 69–70, 275–279.

579 Fischer, M.P., Higuera-Díaz, I.C., Evans, M. A., Perry, E.C., Lefticariu, L., 2009. Fracture-controlled
580   paleohydrology in a map-scale detachment fold: Insights from the analysis of fluid inclusions in
581   calcite and quartz veins. J. Struct. Geol. 31, 1490–1510.

582 Fischer, M.P., Jackson, P.B., 1999. Stratigraphic controls on eformation patterns in fault-related folds: a
583   detachment fold example from the Sierra Madre Oriental, northeast Mexico. J. Struct. Geol. 21, 613–
584   633.

585 Fischer, M.P., Wilkerson, M.S., 2000. Predicting the orientation of joints from fold shape : Results of
586   pseudo – three-dimensional modeling and curvature analysis. Geology 28, 15–18.

587 Fitz-Diaz, E., Hudleston, P., Siebenaller, L., Kirschner, D., Camprubí, A., Tolson, G., Puig, T.P., 2011. Insights
588   into fluid flow and water-rock interaction during deformation of carbonate sequences in the
589   Mexican fold-thrust belt. J. Struct. Geol. 33, 1237–1253.

590 Gale, J.F.W., Reed, R.M., Holder, J., 2007. Natural fractures in the Barnett Shale and their importance for
591   hydraulic fracture treatments. Am. Assoc. Pet. Geol. Bull. 91, 603–622.

592 Hathaway, J. C., Degens, E.G., 1969. Methane-derived marine carbonates of Pleistocene age. Science 165,
593   690–692.

594 Hervouët, Y., Espurt, N., Dhont, D., 2005. Failles normales Paléocène à Lutétien en zone sud-pyrénéenne
595   (Aragon, Espagne) et flexuration de la plaque ibérique. Comptes Rendus Geoscience 337, 385–392.

596 Henderson, I.H.C., McCaig, A. M., 1996. Fluid pressure and salinity variations in shear zone-related veins,
597   central Pyrenees, France: Implications for the fault-valve model. Tectonophysics 262, 321–348.

598 Hilgers, C., Koehn, D., Bons, P.D., Urai, J.L., 2001. Development of crystal morphology during unitaxial
599   growth in a progressively widening vein : II . Numerical simulations of the evolution of antitaxial
600   fibrous veins. Jou. Struc. Geol. 23, 873–885.

601 Hogan, P.J., Burbank, D.W., 1996. Evolution of the Jaca piggyback basin and emergence of the External
602   Sierras, southern Pyrenees. In: P.F. Friend and C.J. Dabrio (Editors), Tertiary Basins of Spain.
603   Cambridge Univ. Press, 153-160.

604 Huyghe, D., Mouthereau, F., Castelltort, S., Filleaudeau, P-Y., Emmanuel, L, 2009. Paleogene propagation of
605   the southern Pyrenean thrust wedge revealed by finite strain analysis in frontal thrust sheets:
606   implications for mountain building. Earth and Planetary Science Letters 288, 421-433.

607

608 Huyghe, D., Castelltort, S., Mouthereau, F., Serra-Kiel, J., Filleaudeau, P.-Y., Berthier, B., Emmanuel, L.,
609   Renard, M., 2012a. Large scale facies change in the middle Eocene South-Pyrenean foreland basin:
610   The role of tectonics and prelude to Cenozoic ice-ages. Sedimentary Geology 253-254, 25-46.

611

612 Huyghe, D., Mouthereau, F., Emmanuel, L., 2012b. Oxygen isotopes of marine mollusc shells record Eocene
613   elevation change in the Pyrenees. Earth and Planetary Science Letters 345-348, 131-141.

614

615 Jolivet, M., Labaume, P., Monie, P., Brunel, M., Arnaud, N., Campani, M., 2007. Thermochronology
616   constraints for the propagation sequence of the south Pyrenean basement thrust system (France-
617   Spain), Tectonics 26, TC5007, doi:10.1029/2006TC002080.

618 Katz, D. A., Eberli, G.P., Swart, P.K., Smith, L.B., 2006. Tectonic-hydrothermal brecciation associated with
619   calcite precipitation and permeability destruction in Mississippian carbonate reservoirs, Montana
620   and Wyoming. Am. Assoc. Pet. Geol. Bull. 90, 1803–1841.

621 Kim, S.-T., O'Neil, J.R., 1997. Equilibrium and nonequilibrium oxygen isotope effects in synthetic
622   carbonates. Geochim. Cosmochim. Acta 61, 3461–3475.

623 Lacombe O., Swennen R., Caracausi A. (eds), 2014. Thematic Issue :Fluid-rock-tectonics interactions in
624   basins and orogens. Marine and Petroleum Geology, 55, 1-332

625 Lacombe O, Tavani S., Soto R. (eds), 2012. Thematic Issue : Into the deformation history of folded rocks.
626   Tectonophysics, 576-577, 1-216

627 Lacombe O., 2012. Do fault slip data inversions actually yield 'paleostresses' that can be compared with
628   contemporary stresses ? A critical discussion. Comptes Rendus Geoscience 344, 159-173.

629   Lacombe, O., Bellahsen, N., Mouthereau, F., 2011. Fracture patterns in the Zagros Simply Folded Belt (Fars,
630   Iran): constraints on early collisional tectonic history and role of basement faults. Geological
631   Magazine, thematic issue « Geodynamic evolution of the Zagros », O. Lacombe, B. Grasemann and G.
632   Simpson (eds), 148, 940-963.

633   Lacroix, B., Buatier, M., Labaume, P., Travé, a., Dubois, M., Charpentier, D., Ventalon, S., Convert-Gaubier, D.,
634   2011. Microtectonic and geochemical characterization of thrusting in a foreland basin: Example of
635   the South-Pyrenean orogenic wedge (Spain). Journal of Structural Geology 33, 1359–1377.

636   Lacroix, B., Travé, A., Buatier, M., Labaume, P., Vennemann, T., Dubois, M., 2014. Syntectonic fluid-flow
637   along thrust faults: Example of the South-Pyrenean fold-and-thrust belt. Marine and Petroleum
638   Geology 49, 84–98.

639   Laubach, S.E., Olson, J., Gross, M.R., 2009. Mechanical and fracture stratigraphy. AAPG Bulletin 93, 1413–
640   1427.

641   Machel, H.G., 2000. Application of Cathodoluminescence to carbonate diagenesis. In: Pagel, M., Barbin, V.,
642   Blanc, P., Ohnenstetter, D. (eds.), Cathodoluminescence in Geosciences. Springer-Verlag, Heigelberg,
643   Germany, 271-302.

644   Machel, H.G., Cavel, P.A., 1999. Low-flux, tectonically-induced squeegee fluid flow (« hot flash ») into the
645   Rocky Mountain Foreland Basin. Bulletin of Canadian Petroleum Geology 47, 510-533.

646   McCaig, A.M., Tritlla, J., and Banks, D., 2000, Fluid flow patterns during Pyrenean thrusting. Journal of
647   Geochemical Exploration 69-70, 539–543.

648   McCaig, A.M., Wayne, D.M., Marshall, J.D., Banks, D., Henderson, I., 1995. Isotopic and fluid inclusion studies
649   of fluid movement along the Gavarnie Thrust, central Pyrenees: reaction front in carbonate
650   mylonites. American Journal of Science 295, 309-343.

651   Millán, H., 1996. Estructura y cinematica del frente de cabalgamiento surpirenaico, Sierras Exteriores
652   aragonesas, PhD Thesis, Universidad de Zaragoza, Spain, 330 pp.
653
654   Millán, H., Aurell, M., Meléndez, A., 1994. Synchronous detachment folds and coeval sedimentation in the
655   Prepyrenean External Sierras (Spain): a case study for a tectonic origin of sequences and systems
656   tracts. Sedimentology 41, 1001-1024.
657
658   Molina, E., Ortiz, N., Serra-Kiel, J., 1988. Implicationes paleoecologicas de los foraminiferos en el Eocene
659   del Prepirineo oscense (sector de Arguís). Revista Espanola de Paleontologia 3, 45-57.

660   Morley, C.K., Warren, J., Tingay, M., Boonyasaknanon, P., and Julapour, A., 2014, Comparison of modern
661   fluid distribution, pressure and flow in sediments associated with anticlines growing in deepwater
662   (Brunei) and continental environments (Iran): Marine and Petroleum Geology, thematic issue on
663   fluid-rock-tectonics interactions in basins and orogens. , Lacombe O., Swennen R., Caracausi A. (eds),
664   55, 230–249, doi: 10.1016/j.marpetgeo.2013.11.011.

665   Nalpas, T., Gapais, D., Verges, J., Barrier, L., Gestain, V., Leroux, G., Rouby,D., Kermarrec, J.J., 2003. Effects of
666   rate and nature of synkinematic sedimentation on the growth of compressive structures constrained
667   by analogue models and field examples. Geol. Soc. Lond. Spec. Publ. 208, 307–319.

668   Novoa, E., Suppe, J., Shaw, J.H., 2000. Inclined-shear resto- ration of growth folds. AAPG Bull. 84, 787–804.

669   Oliva-Urcia, B., Pueyo, E., 2007. Rotational basement kinematics deducted from remagnetized cover rocks
670   (Internal Sierras, southwestern Pyrenees). Tectonics 26, TC4014, doi:10.1029/2006TC001955.

671 Poblet, J., Hardy, S., 1995. Reverse modelling of detachment folds; application to the Pico del Aguila
672   anticline in the South Central Pyrenees (Spain). Journal of Structural Geology 17, 12, 1707 – 1724.

673 Poblet, J., Muñoz, J., Travé, A., and Sierra-Kiel, J., 1998. Quantifying the kinematics of detachment folds
674   using three-dimensional geometry: Application to the Mediano anticline (Pyrenees, Spain). GSA
675   Bulletin 110, 111–12.

676 Pueyo, E.L., Millán, H., Pocoví, A., 2002. Rotation velocity of a thrust: a paleomagnetic study in the External
677   Sierras (Southern Pyrenees). Sedimentary Geology 146, 191-208.

678 Puigdefàbregas, C., 1975. La sedimentación molásica en la cuenca de Jaca. Pirineos 104, 1-188.

679 Pujalte, V., Baceta, J., Schmitz, B., Orue-Etxebarria, X., Payros, A., Bernaola, G., Apellaniz, E., Caballero, F.,
680   Robador, A., Serra-Kiel, J., Tosquella, J., 2009. Redefinition of the Ilerdian Stage (early Eocene).
681   Geologica Acta 7, 177–194.

682 Qing, H., Mountjoy, E., 1992. Large-scale fluid flow in the Middle Devonian Presqu'ile Barrier, Western
683   Canada sedimentary basin. Geology 20, 903–906.

684 Quintà, A., Tavani, S., 2012. The foreland deformation in the south-western Basque–Cantabrian Belt
685   (Spain).Tectonophysics, thematic issue : « Into the deformation history of folded rocks » , O.
686   Lacombe, S. Tavani, R. Soto (eds), , 576-577, 4-19.

687 Ramsay, J., 1980. The crack-seal mechanism of rock deformation. Nature 284, 135–139.

688 Reynolds, T.J., Goldstein, R.H., 1994. Systematics of fluid inclusions in diagenetic minerals, SEPM Short
689   Course.

690 Roedder, E., 1984. Fluid Inclusions. Rewiews in Mineralogy 12, 644 pp.

691 Rosenbaum, J., Sheppard, S.M.F., 1986. An isotopic study of side- rites, dolomites and ankerites at high
692   temperatures. Geochimica et Cosmochimica Acta 50, 1147–1150.

693 Roure, F., Swennen, R., Schneider, F., Faure, J.L., Ferket, H., Guilhaumou, N., Osadetz, K., Robion, P.,
694   Vandeginste, V., 2005. Incidence and Importance of Tectonics and Natural Fluid Migration on
695   Reservoir Evolution in Foreland Fold-And-Thrust Belts. Oil Gas Sci. Technol. 60, 67–106.

696 Savage, H.M., Ryan Shackleton, J., Cooke, M.L., Riedel, J.J., 2010. Insights into fold growth using fold-related
697   joint patterns and mechanical stratigraphy. J. Struct. Geol. 32, 1466–1475.

698 Sztràkos, K., Castelltort, S., 2001. La sédimentologie et les foraminifères bartoniens et priaboniens des
699   coupes d'Arguis (Prépyrénées aragonaises, Espagne). Incidence sur la corrélation des biozones à la
700   limite Bartonien/Priabonien. Revue de Micropaléontologie 44, 233-247.

701 Tavani, S., Storti, F., Fernández, O., Muñoz, J. a., Salvini, F., 2006. 3-D deformation pattern analysis and
702   evolution of the Añisclo anticline, southern Pyrenees. J. Struct. Geol. 28, 695–712.

703 Teixell, A., 1996. The Anso transect of the southern Pyrenees: basement and cover thrust geometries.
704   Journal of the Geological Society. 153, 301-310.

705 Travé, A., Calvet, F., Sans, M., Verges, J., and Thirlwall, M., 2000. Fluid history related to the Alpine
706   compression at the margin of the south-Pyrenean Foreland basin: the El Guix anticline.
707   Tectonophysics, 321, 73–102.

708 Travé, A., Labaume, P., and Vergés, J., 2007, Fluid systems in Foreland Fold-and-Thrust Belts: An overview
709   from the Southern Pyrenees. In: Lacombe, O., Lavé, J., Roure, F., and Vergés, J. eds,, Thrust Belts and
710   Foreland Basins : From Fold Kinematics to Hydrocarbons Systems, Springer, 93–115.

711 Van Geet, M., Swennen, R., Durmishi, C., Roure, F., Muchez, P.H., 2002. Paragenesis of Cretaceous to Eocene
712   carbonate reservoirs in the Ionian fold and thrust belt (Albania): relation between tectonism and
713   fluid flow. Sedimentology 49, 697–718.

714 Vandeginste, V., Swennen, R., Allaeys, M., Ellam, R.M., Osadetz, K., Roure, F., 2012. Challenges of structural
715   diagenesis in foreland fold-and-thrust belts: A case study on paleofluid flow in the Canadian Rocky
716   Mountains West of Calgary. Mar. Pet. Geol. 35, 235–251.

717 Vidal-Royo, O., Koyi, H. A., Muñoz, J.A., 2009. Formation of orogen-perpendicular thrusts due to mechanical
718   contrasts in the basal décollement in the Central External Sierras (Southern Pyrenees, Spain).
719   Journal of Structural Geology 31, 523–539.

720 Vidal-Royo, O., Cardozo, N., Muñoz, J.A. ; Hardy, S., Maerten, L., 2012. Multiple mechanisms driving
721   detachment folding as deduced from 3D reconstruction and geomechanical restoration: the Pico del
722   Aguila anticline (External Sierras, Southern Pyrenees). Basin Research 24, 294-313.

723 Vidal-Royo, O., Munoz, J.A., Hardy, S., Koyi, H., Cardozo, N., 2013. Structural evolution of the Pico del Águila
724   anticline (external Sierras, southern Pyrenees) derived from sandbox, numerical and 3D structural
725   modelling Techniques. Geologica Acta 11, 1–26.

726 Zamarreño, I., Anadón, P., Utrilla, R., 1997. Sedimentology and isotopic composition of Upper Palaeocene
727   to Eocene non-marine stromatolites, eastern Ebro Basin, NE Spain. Sedimentology 44, 159–176.

728

729 Captions

730 Figure 1: A- Regional geological map of the Southern Central Pyrenees with location of

731 the balanced cross-sections that cross the Pico del Aguila anticline (Huyghe et al., 2009);

732 B- Stratigraphic column for the Pico del Aguila area (after Castelltort et al., 2003).

733 Lithological key of patterns from bottom to top: carets – evaporate, dashs – clay,

734 parallelograms – dolostone, rectangles – limestone, big dots in irregular shapes – river

735 conglomerates, plain black – marls, fine dots - sandstone; C- Transverse and longitudinal

736 regional cross-sections in the Sierras Exteriores, focusing on the Pico del Aguila Area

737 (Huyghe et al., 2009).

738

739 Figure 2: Geological map of the Pico del Aguila Anticline based on previously published

740 maps (Puigdefabregas, 1975; Millán, 1996; Vidal-Royo et al., 2012), aerial photographs

741 and new field observation and measurements. A balanced cross-section following line C-

742 C' is presented, with a length balance of layers for strata younger than Triassic and an

743 area balance for the Triassic rocks of the décollement. Dotted frames on the maps are

744 areas of maps presented in figures 4-6. White-labeled black dots locate fracture

745 measurement sites or sample sites for geochemical analyses. Please refer to

746 supplementary material 2 for GPS values. In the stratigraphy caption box, "cont." refers

747 to continental environment.

748

749 Figure 3: Photomicrographs of thin- and thick-sections using polarized and cross-

750 polaryzed microscopy. a – Multiple crack-seals and fibrous vein where calcite crystals

751 exhibit the growth direction, recording a mixed mode I-mode II 'transtensional' opening

752 mode of the vein (sample A14); b – Vein with elongated blocky calcite texture where the

753 grain growth direction is perpendicular to the border of the vein, indicating a mode I

754 opening (sample A44). c – Photomicrograph of fluid inclusions in a thick-section. Biggest

755 primary or pseudo-secondary fluid inclusions are circled in red and the stained parts in

756 crystals corresponds to an increase in density of secondary fluid inclusion trails (sample

757 A45). d – Calcite vein with blocky texture fringed by microsparitic crystals, recording a

758 two-stage opening of the vein (sample A86), analogous to the crack-seal model (Ramsay,

759 1980).

760

23

761 Figure 4: Results of fracture analysis in the Triassic to Lutetian prefolding strata in the
762 anticline. Results are presented on 3 diagrams (Schmidt' lower-hemisphere, equal-area
763 stereonets) displaying raw data in current strata attitude (left), then corrected for fold
764 axial plunge related to the Gavarnie thrust activation (middle), and corrected for local
765 bedding dip (right). Location of the measurement area is given in Fig. 2 and in
766 supplementary material 2. Abbreviations on the map are for the formations: Ar – Arguis
767 Fm., Gu – Guara Fm., Tp – Tremp Fm., A-B – Adraen Bona Fm., Tr – Triassic Fms.

768

769 Figure 5: Results of fracture analysis in the western syncline located in the Pico del
770 Aguila area. Same key as in Fig. 4. Abbreviations on the map are for formations: Ar –
771 Arguis Fm., Gu – Guara Fm., Tp – Tremp Fm., A-B – Adraen Bona Fm.

772

773 Figure 6: Results of fracture analysis in the syn-folding and post-folding strata of
774 Bartonian to Priabonian age, respectively. Same key as in Fig. 4. Abbreviations on the
775 map are for formations: Cp – Campodarbe Fm., B-A – Beslusé Atares Fm., Ar – Arguis
776 Fm., Gu – Guara Fm.

777

778 Figure 7: Results of fault-slip inversion (Schmidt' stereonets lower hemisphere).
779 Computed stress axes are reported as stars with three branches (σ_1), four branches (σ_2)
780 and five branches (σ_3). Convergent/divergent black arrows indicate the direction of
781 compression/tension. Results are represented in the current attitude of strata, and
782 diagrams labeled as "corrected" correspond to the same computed tensor and fault-slip
783 data but corrected for removal of fold axial plunge related to the activation of Gavarnie
784 thrust. Diagrams labeled as "unbasc" are corrected for fold axis plunge then for bed tilt.
785 Diagrams are gathered according to consistency of reconstructed paleostress tensors.
786 Abbreviations on the map are for formations: Cp – Campodarbe Fm., B-A – Belsué Atares
787 Fm., Ar – Arguis Fm., Gu – Guara Fm., Tp – Tremp Fm., A-B – Adraen Bona Fm., Tr –
788 Triassic Fms.

789

790 Figure 8: a-d – Field photographs with chronological interpretations of fracture
791 networks. Sites for photographs: site 39(a), site 497 (b), site 476 (c), and site 447(d). e-f
792 – Photographs of faults and fractures showing the spacing and vertical persistence of
793 fractures observed at site 433 (refer to Figs. 4 to 7 for location).

24

794

795 Figure 9: Photomicrographs of thin sections under cathodoluminescence microscopy: a

796 – Heterogeneous blocky-type calcite in vein, with brightness variation related to crystal

797 boundaries or to atomic-scale defects (sample A77); b - Heterogeneous blocky-type

798 calcite in vein exhibiting bright to dull orange zonation related to crystal growth (sample

799 A37); c – Elongated blocky-type calcite in vein exhibiting brightness variation related to

800 crystals (sample A44, Fig. 3-b). Please refer to the electronic version for colors.

801

802 Figure 10: Results of $\delta^{18}O$ and $\delta^{13}C$ analysis of veins and host-rocks displayed in context

803 of fracture age with respect to folding. a - $\delta^{18}O$ vs $\delta^{13}C$ plot, b - $\delta^{18}O$ of veins vs $\delta^{18}O$ of

804 related host-rocks. On all charts, solid symbols are for vein cements and fault coatings,

805 whereas empty symbol are for related host-rocks samples. Please refer to the text for

806 the explanation of labels *(1)* to *(4)*. All values are expressed in ‰PDB. Labels XX/YY

807 refers to the number of analyzes performed / number of samples collected. See Table 2

808 and Supplementary Table S1 for detailed isotopic data.

809

810 Figure 11: Schematic block diagrams of structural, sedimentary and mesostructural

811 evolutionary scenario of the Pico del Aguila anticline. Fracture sets and related

812 contractional/extensional trends are illustrated. Stratigraphic timing and timing with

813 respect to folding stated for each block diagram. Fractures are not represented

814 according to abundance. Labels (1) to (5) are related to local and regional stress

815 orientations (see text).

816

817 Figure 12: a - Schematic cross-section illustrating evolution of the paleo-fluid system in

818 the Pico del Aiguila Anticline. b - Comparison with the Sheep Mountain anticline,

819 Wyoming, USA (after Beaudoin et al., 2011; Evans and Fischer, 2012).

820

821 Table 1: Results of the statistical interpretation of fracture set orientation, stratigraphic

822 distribution and indicators for relative chronology.

823

824 Table 2: Number of samples used for isotopic analysis in each formation, along with the

825 related range of isotopic values measured.

826

827   Table S1: Results of isotopic analyses.

828   Table S2: Geographical location of samples and measurement sites

829

Set name	Set strike*	Set inclination	Stratigraphic units	Evidence for relative age
J1	120	bed-normal	Guara - lower Arguis	RD, CC, A
J2	90	bed-normal	Guara	RD, CC, A
J3	70	bed-normal	All	CC, A
J4	40	bed-normal	All	CC, A
J5	170	sub bed-normal	All	CC, A

*: mean strike within 10° computed statistically

RD: Restricted to Stratigraphic units CC: cross-cutting relationships; A: respect andersonian criterion

Age relative to folding	Formation		number of analyses/number of samples	Range of isotopic values (>80% samples)	
				$\delta^{18}O$ (‰PDB)	$\delta^{13}C$ (‰PDB)
Post-folding	Campodarbe	veins	7/8	-2.20 to -0.02	-1.77 to -0.77
		host-rock	7/8	-6.05 to -5.4	-1.2 to 0.05
Syn-folding	Belsue Atares	veins	2/3	-4.65 to -2.91	-2.61 to -1.38
		host-rock	3/3	-5.81 to -4.81	-1.53 to 0.11
	Arguis	veins	25/25	-4.35 to -0.66	-1.64 to 0.48
		host-rock	20/25	-4.47 to -2.55	-1.7 to 0.43
	Guara	veins	29/29	-10.4 to -1.42	-0.05 to 2.25
		host-rock	20/29	-6.7 to -1.42	-1.5 to 2.15
Pre-folding	Tremp	veins	3/3	-7.26 to -6.71	-7.77 to -6.34
		host-rock	1/3	-3.77	-6.29
	Adraen Bona	veins	1/1	-5.43	-0.56
		host-rock	1/1	-3.9	1.49
	Triassic	veins	3/4	-7.65 to -6.73	-5.43 to -3.51
		host-rock	4/4	-5.78 to -3.28	-1.37 to 2.65

Legend (map a):

- Upper Cretaceous
- Triassic
- Paleozoic basement
- Hecho Group turbidites (Eocene)
- Cuisian - Lutetian
- Priabonian
- Bartonian
- Miocene
- Oligocene

A' ···· A Cross section — Faults — — Buried Faults ········· Fold axis

Stratigraphic column (b):

		Campodarbe Conglomerates
Post-folding	OLIG.	3000 m
Folding	EOCENE PRIAB. BARTONIAN	Belsué - Atarès Sandstones
		2000 m Arguis Marls
Pre-folding	LUTETIAN	Guara Limestones 1000 m
	Paleoc. L. Cret.	Tremp Fm. Adraen Bona Limestones
	TRIASSIC	0 m

Cross sections (c):

A — Rio Guarga Syncline — Arguis Syncline (B B') — Ebro basin — A'

B — Rasal — Bentué de Rasal — (A A') Pico del Aguila — Gabardiella Lusara — B'

Cross section legend:

- Upper Cretaceous - Lower Paleocene and Triassic detachment unit
- Paleozoic basement
- Bartonian
- Guara Limestone Fm Cuisian - Lutetian
- Alveolina Limestone Fm (Lower Eocene)
- Faults
- Upper Eocene - Miocene continental

Belsué-Atarès Fm

Site 459
J4
J3
17

Site 446
J4
21

Site 464
J4
10

Site 137-2
U
J4
26

Site 137
U
J3
14

Campodarbe Fm

Site 528
J4
J3
15

Site 144
J3
18

Site 144-2
U
17

Site 146
J4
24

Site 449
J4
28

Site 447
J5
J4
U
38

Arguis Fm

Site 145
U
J4
J3
25

Site 433-2
J4
J3
10

Site 44
J3
10

Site 434
J3
11

Site 433-1
U
15

Site 44-2
J3
11

Site 476
J4
J2
31

Site 43
J3
16

Site 136
J5
J3
19

Syn-folding E-W extension (set F1)
Site 433(1) — current / corrected
Site 26(1) — current / corrected
Site 27 — current / corrected
Site 52 — current / corrected
Site 33(2) — current / corrected

Post-folding activation E-W compression (set F2)
Site 26(2)
Site 434 / Site 433(2)
Site 474 — current / unbasc
Site 33(1) — current / corrected

Post-thrust activation NE-SW compression
Site 447 / Site 444(1)

Post-thrust activation N-S compression (set F3)
Site 136(1) / Site 136(2) / Site 34 / Site 444(2) / Site 25

Cd
B-A
Ag
Gu
A-B
Tr
Tp

447
136
433 · 434
444
34
26
27 · 474
33 · 25
52

a — Host-rock · Vein · atomic-scale defects (twins) · grain boundaries · 4 mm

b — Host-rock · growth zonation · Vein · 2 mm

c — Host-rock · Vein · 1 mm

a
Pre-folding (Upper Lutetian)

Set J1 (~090°) *
initial orientation of folding axis
Set J2 (~045°) *
(1)
(2)
(2)
(1)
N

b
Early syn-folding (Bartonian)

Set J3 (045°) *
(2)
Set J1 (~100°)*
Set J2 (060°) *

c
Late syn-folding (Priabonian)

Set J5 (160°)
Set J4 (045°)
(2)
(3)
Set F1 (N-S Normal faults)
Set J1 (120°)
Set J2 (080°)
Set J3 (060°)

d
Post-folding Thrusting (Oligocene)

Set F1 (N-S Normal faults)
Reactivation of sets J3-J4 by (4)
(5)
30°
Set F3 (E-W Reverse faults)
(4)
Reactivation of set J5 by (4)
Set F2 (N-S Reverse faults)
Set J1 (120°)
Set J2 (080°)
Set J3 (060°)
Set J4 (045°)

a - Pico del Aguila Anticline paleo-fluid system
   (Syn-depositional décollement folding at shallow depth <1 km)

b - Sheep Mountain Anticline paleo-fluid system (Beaudoin et al., 2011)
   (Post-compaction basement-cored folding at depth >2 km)

post-folding

syn-folding

pre-folding

syn-folding sets
break seal

Layer Parallel Shortening sets
stratified system

-?-

Basement

syn-folding set enhanced
cover-scale permeability

Madison-Phosphoria reservoir

Basement

fluid system -arrows for direction of migration-

Formational fluids

local   inter-formational

Exotic fluids

Meteoric fluids   hydrothermal fluids

Permeable sandstones formations

Fractured limestones formations

Non-permeable shaly/evaporite formations

Highlights:

. Fluid system deciphered during syn-sedimentary folding

. Role of tectonic and sedimentary environment on fluid system evolution

. Role of burial on vertical permeability of fractures

. Fracture development witnesses fold rotation around a vertical axis

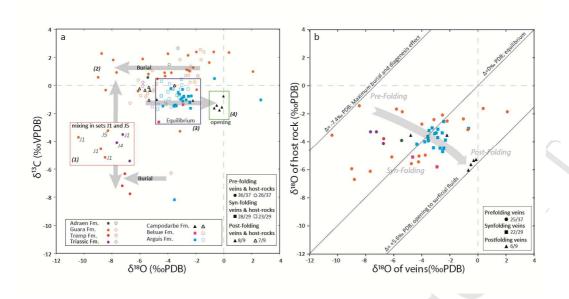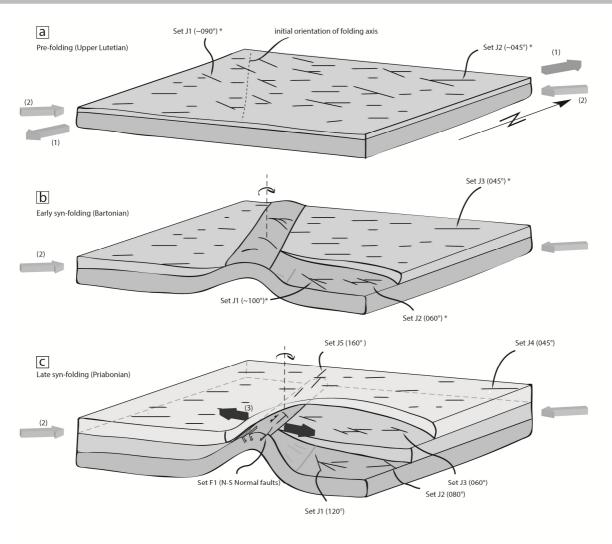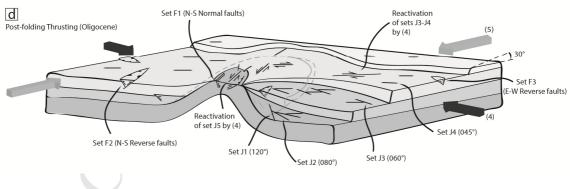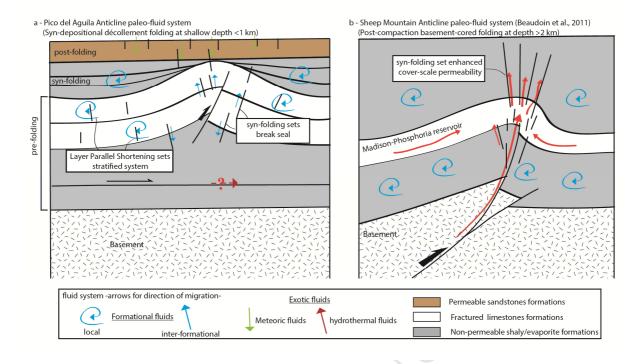| Deposition regarding folding	Sample	Formation	Age	Fracture Set	Vein isotopic ratios		Host rock isotopic ratio		Site Number (Figure for location)
					$\partial^{18}O$	$\partial^{13}C$	$\partial^{18}O$	$\partial^{13}C$	
Post-folding	A040	Campodarbe	Priabonian	Set J4			-5.36	-0.13	447 (Fig. 6)
	A041	Campodarbe	Priabonian	Set J5	-0.3	-1.77	-5.35	-1.06	449 (Fig. 6)
	A042	Campodarbe	Priabonian	Set J5	-0.68	-1.62	-6.03	-0.24	450 (Fig. 6)
	A044	Campodarbe	Priabonian	Set J4	-0.13	-1.56	-5.28	-0.36	452 (Fig. 6)
	A045	Campodarbe	Priabonian	Set J4	-0.5	-1.43	-5.64	-0.34	453 (Fig. 6)
	A048	Campodarbe	Priabonian	Set J3	-0.02	-0.77			455 (Fig. 6)
	A050	Campodarbe	Priabonian	Set J4	-2.2	-1.08	-3.52	-0.02	458 (Fig. 6)
	A050	Campodarbe	Priabonian	Set J2	-4.79	-1.02	-3.52	-0.02	458 (Fig. 6)
Syn-folding	A103	Belsue-Atarès	Bartonian	Set J3			-4.81	0.11	507 (Fig. 4)
	A054	Belsue-Atarès	Bartonian	Set J3	-2.91	-1.38	-5.81	-0.05	465 (Fig. 4)
	A104	Belsue-Atarès	Bartonian	Set J2	-4.65	-2.61	-5.11	-1.53	511 (Fig. 4)
	A001	Arguis	Bartonian	Set J2	-3.48	-1.41	-3.19	-0.9	433 (Fig. 4)
	A003	Arguis	Bartonian	Set F1	-3.53	-8.19	-3.91	-0.97	433 (Fig. 7)
	A004	Arguis	Bartonian	Set F1	-3.4	-1.47			433 (Fig. 7)
	A005	Arguis	Bartonian	Set F1	-3.55	-1.49	-3.77	-1.55	433 (Fig. 7)
	A008	Arguis	Bartonian	Set J3	-4.35	-1.48	-4.16	-1.14	433 (Fig. 4)
	A009	Arguis	Bartonian	Set F1	2.66	-1.04			433 (Fig. 7)
	A010	Arguis	Bartonian	Set F1	-3.26	-0.51	-3	0.02	433 (Fig. 7)
	A011	Arguis	Bartonian	Set J2	-2.31	-0.76	-3.87	0.12	433 (Fig. 4)
	A012	Arguis	Bartonian	Set F1	-2.54	-0.78	-3.35	-0.72	433 (Fig. 7)
	A013	Arguis	Bartonian	Set J2	-2.51	-0.78	-4.72	-1.7	433 (Fig. 4)
	A013	Arguis	Bartonian	Set J2	-2.51	-0.78	-4.67	-1.37	433 (Fig. 4)
	A015	Arguis	Bartonian	Set J1	-2.94	-0.29			434 (Fig. 4)
	A020	Arguis	Bartonian	Set J4	-3.79	-0.23	-3.99	-0.46	436 (Fig. 4)
	A021	Arguis	Bartonian	Set J3	-2.86	-0.77	-3.69	-0.29	436 (Fig. 4)
	A022	Arguis	Bartonian	Set F2	-2.96	-0.9	-3.35	-0.72	439 (Fig. 7)
	A071	Arguis	Bartonian	Set J2	-3.56	-1.46	-3.61	-0.23	476 (Fig. 4)
	A072	Arguis	Bartonian	Set J2	-2.43	-1.19	-2.55	-0.26	476 (Fig. 4)
	A073	Arguis	Bartonian	Set J3	-2.85	-0.82	-3.09	-0.28	477 (Fig. 4)
	A077	Arguis	Bartonian	Set J2	-2.7	-1.04	-4.47	-0.75	482 (Fig. 4)
	A077	Arguis	Bartonian	Set J3	-2.43	-1.23	-4.47	-0.75	482 (Fig. 4)
	A078	Arguis	Bartonian	Set J3	-2.37	-1.64			482 (Fig. 4)
	A107	Arguis	Bartonian	Set J3	-2.93	-1.13			513 (Fig. 4)
	A121	Arguis	Bartonian	Set F3	-0.66	0.48	-3.03	0.43	522 (Fig. 7)
	A124	Arguis	Bartonian	Set F2	-3.16	-0.64	-4.45	0.28	523 (Fig. 7)
	A128	Arguis	Bartonian	Set J2	-3.08	-1.00	-3.4	-1.44	527 (Fig. 4)
Pre-folding	A031	Guara	Lutetian	Set F2	-5.8	1.88	-1.66	2.55	444 (Fig. 7)
	A032	Guara	Lutetian	Set F3	-8.45	-0.34	-1.42	2.38	445 (Fig. 7)
	A033	Guara	Lutetian	Set F3	-3.99	2.25	-2.73	0.69	445 (Fig. 7)
	A037	Guara	Lutetian	Set J2	0.38	2.34	-1.62	1.83	445 (Fig. 4)
	A056	Guara	Lutetian	Set J3	-8.99	0.57	-5.94	-0.74	467 (Fig. 4)
	A057	Guara	Lutetian	Set J5	-4.19	0.66	-5.04	-0.41	467 (Fig. 4)
	A060	Guara	Lutetian	Set J5	-4.23	0.9	-5.45	-0.59	467 (Fig. 4)
	A060	Guara	Lutetian	Set J5	-3.75	0.9	-4.97	-0.27	467 (Fig. 4)
	A061	Guara	Lutetian	Set J5	-4.74	0.46	-5.58	-0.82	469 (Fig. 4)
	A064	Guara	Lutetian	Set J2	-2.52	1.07	-2.08	0.23	470 (Fig. 4)
	A064	Guara	Lutetian	Set J2	-2.66	1.12			470 (Fig. 4)
	A064	Guara	Lutetian	Set J5	-8.29	-3.24			470 (Fig. 4)
	A066	Guara	Lutetian	Set J3	-2.42	1.01			472 (Fig. 4)
	A066	Guara	Lutetian	Set J3	-1.94	-0.31			472 (Fig. 4)
	A067	Guara	Lutetian	Set J1	-10.4	-3.71	-3.52	-0.02	473 (Fig. 4)
	A068	Guara	Lutetian	Set J3	-1.03	1.62	-2.36	1.36	474 (Fig. 4)
	A070	Guara	Lutetian	Set J3	-2.19	1.26	-2.51	0.72	475 (Fig. 4)
	A087	Guara	Lutetian	Set J5	-6.14	-0.41	-5.1	1.05	497 (Fig. 4)
	A088	Guara	Lutetian	Set J1	-8.49	-5.17			497 (Fig. 4)
	A089	Guara	Lutetian	Set J3	-7.91	1.81			498 (Fig. 4)
	A091	Guara	Lutetian	Set J2	-7.67	0.92	-6.12	0.38	503 (Fig. 4)
	A094	Guara	Lutetian	Set J1	-8.8	-4.56	-6.7	-1.27	499 (Fig. 4)
	A097	Guara	Lutetian	???	-3.13	-3.28	-2.41	0.22	503 (Fig. 4)
	A100	Guara	Lutetian	???	-5.39	0.8	-1.85	0.67	503 (Fig. 4)
	A100	Guara	Lutetian	Set J2	2.1	0.98	-1.85	0.67	503 (Fig. 4)
	A109	Guara	Lutetian	Set J3	-0.71	2.38	-3.12	1.83	515 (Fig. 4)
	A115	Guara	Lutetian	Set J3	-8.74	2.27			519 (Fig. 4)
	A118	Guara	Lutetian	Set J5	-1.96	2.38			520 (Fig. 4)
	A119	Guara	Lutetian	???	-2.55	2.14			520 (Fig. 4)
	A086	Adraen-Bona	Cretaceous	Set J2	-5.43	0.56	-3.9	1.49	493 (Fig. 4)
	A082	Tremp	Cretaceous	Set J5	-7.08	-6.34			489 (Fig. 4)
	A083	Tremp	Cretaceous	Set J5	-7.26	-7.2			489 (Fig. 4)
	A084	Tremp	Cretaceous	Set J4	-6.71	-7.77	-3.77	-6.29	490 (Fig. 4)
	A131	Triassic	Triassic	Set J1	-7.23	-3.51	-3.28	2.65	553 (Fig. 4)
	A131	Triassic	Triassic	Set J4	-7.65	-4.09	-3.28	2.65	553 (Fig. 4)
	A132	Triassic	Triassic	???	-6.73	-5.43	-4.11	-1.37	555 (Fig. 4)
	A133	Triassic	Triassic				-5.78	0.21	555 (Fig. 4)

Accuracy of the measurments reported in this table is based on the standard deviation of the values obtained from the standards, and is of 0.05‰ for carbon and 0.1‰ for oxygen

Supplementary material 2: Site number lo cation

Site number	Longitude (decimal)	Latitude (decimal)	Formation	Age
446	-0.398945	42.327804	Campodarbe	Priabonian
447	-0.407133	42.330704	Campodarbe	Priabonian
449	-0.402130	42.329652	Campodarbe	Priabonian
450	-0.401991	42.329628	Campodarbe	Priabonian
452	-0.401818	42.329522	Campodarbe	Priabonian
453	-0.401759	42.329546	Campodarbe	Priabonian
455	-0.401005	42.329284	Campodarbe	Priabonian
458	-0.400551	42.329169	Campodarbe	Priabonian
528	-0.393591	42.342126	Campodarbe	Priabonian
459	-0.393884	42.325935	Belsué-Atarès	Bartonian
464	-0.394159	42.325990	Belsué-Atarès	Bartonian
465	-0.394251	42.326038	Belsué-Atarès	Bartonian
507	-0.412320	42.328541	Belsué-Atarès	Bartonian
511	-0.412357	42.328458	Belsué-Atarès	Bartonian
43	-0.414050	42.326917	Arguis	Bartonian
44	-0.426783	42.325333	Arguis	Bartonian
433	-0.413300	42.326370	Arguis	Bartonian
434	-0.411983	42.326212	Arguis	Bartonian
436	-0.414191	42.326608	Arguis	Bartonian
439	-0.414035	42.326563	Arguis	Bartonian
476	-0.412080	42.326619	Arguis	Bartonian
477	-0.412371	42.326508	Arguis	Bartonian
482	-0.412419	42.327050	Arguis	Bartonian
513	-0.412389	42.326222	Arguis	Bartonian
522	-0.420804	42.327150	Arguis	Bartonian
523	-0.421153	42.327128	Arguis	Bartonian
527	-0.424152	42.325338	Arguis	Bartonian
25	-0.40305	42.305800	Guara	Lutetian
26	-0.40723	42.314360	Guara	Lutetian
27	-0.407833	42.314367	Guara	Lutetian
28	-0.406483	42.313517	Guara	Lutetian
31	-0.404667	42.308367	Guara	Lutetian
32	-0.403767	42.307033	Guara	Lutetian
33	-0.403067	42.305917	Guara	Lutetian
34	-0.410050	42.323300	Guara	Lutetian
35	-0.414367	42.324433	Guara	Lutetian
36	-0.428350	42.297539	Guara	Lutetian
37	-0.426886	42.298922	Guara	Lutetian
38	-0.428286	42.301444	Guara	Lutetian
39	-0.411600	42.317750	Guara	Lutetian
40	-0.412467	42.321100	Guara	Lutetian
42	-0.414767	42.322667	Guara	Lutetian
45	-0.411300	42.325400	Guara	Lutetian
46	-0.422067	42.306017	Guara	Lutetian
51	-0.409400	42.309736	Guara	Lutetian
52	-0.402764	24.300739	Guara	Lutetian
136	-0.412183	42.326367	Guara	Lutetian
137	-0.411233	42.329683	Guara	Lutetian
138	-0.428667	42.305850	Guara	Lutetian
139	-0.448000	42.303667	Guara	Lutetian
141	-0.446800	42.294267	Guara	Lutetian
142	-0.442767	42.310567	Guara	Lutetian
144	-0.393750	42.345333	Guara	Lutetian
145	-0.418917	42.324983	Guara	Lutetian
146	-0.402833	42.335867	Guara	Lutetian
444	-0.412102	42.325097	Guara	Lutetian
445	-0.412098	42.325157	Guara	Lutetian
467	-0.405834	42.312462	Guara	Lutetian
469	-0.405920	42.312555	Guara	Lutetian
470	-0.405842	42.312665	Guara	Lutetian
472	-0.405998	42.312688	Guara	Lutetian
473	-0.406108	42.312823	Guara	Lutetian
474	-0.406552	42.313484	Guara	Lutetian
475	-0.406526	42.313602	Guara	Lutetian
497	-0.419564	42.306512	Guara	Lutetian
498	-0.420014	42.306393	Guara	Lutetian
499	-0.420358	42.306254	Guara	Lutetian
500	-0.429013	42.304032	Guara	Lutetian
503	-0.403275	42.306514	Guara	Lutetian
515	-0.416279	42.323905	Guara	Lutetian
519	-0.414092	42.322768	Guara	Lutetian
520	-0.412027	42.319628	Guara	Lutetian
493	-0.411017	42.309405	Adrean-Bona	Cretaceous
489	-0.407789	42.310467	Tremp	Cretaceous
490	-0.407872	42.310662	Tremp	Cretaceous
553	-0.401047	42.285117	Triassic	Triassic
555	-0.401272	42.286006	Triassic	Triassic

Site number in italic: site where samples for isotopic analysis were taken